Volume 14
Number 7
7 April 2024
Pages 1693–2014

Catalysis Science & Technology

rsc.li/catalysis

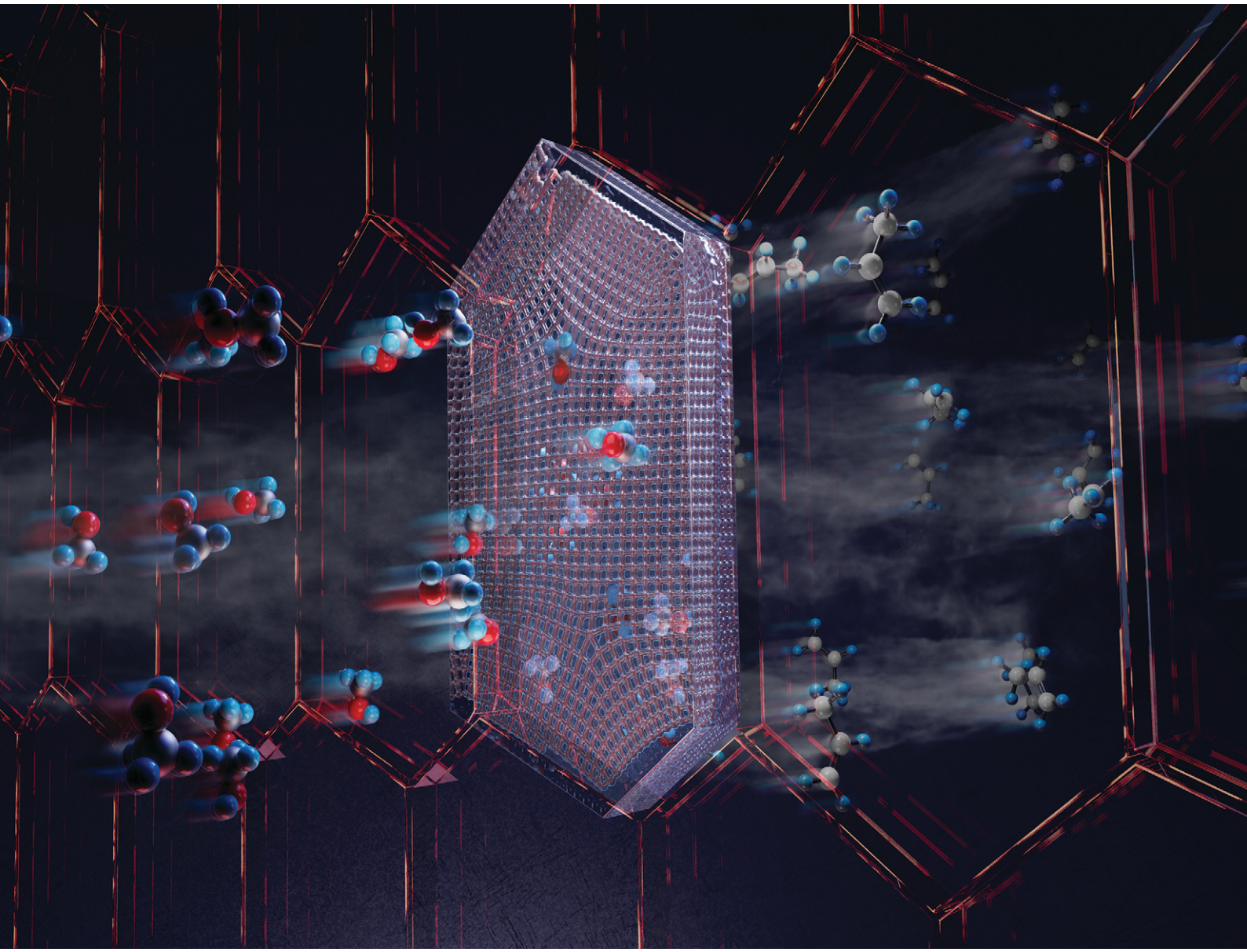

ISSN 2044-4761

ROYAL SOCIETY OF CHEMISTRY

PAPER

Zhiwei Wu, Yanlong Gu, Jianguo Wang *et al.*
Controlling the morphologies and crystal growth orientations of H-ZSM-5: their impact on the structure-diffusion-performance relationship in the methanol-to-propylene reaction

Catalysis Science & Technology

ROYAL SOCIETY OF CHEMISTRY

PAPER

View Article Online
View Journal | View Issue

Cite this: *Catal. Sci. Technol.*, 2024, **14**, 1760

Controlling the morphologies and crystal growth orientations of H-ZSM-5: their impact on the structure-diffusion-performance relationship in the methanol-to-propylene reaction†

Wei Zhang,‡[ad] Xiaohu Wang,‡[bc] Zhiwei Wu, *[b] Zhikai Li,[b] Xiaojing Yong,[d] Yanlong Gu *[a] and Jianguo Wang*[c]

Received 9th November 2023,
Accepted 18th January 2024

DOI: 10.1039/d3cy01558k

rsc.li/catalysis

In this study, three typical ZSM-5 catalysts with different morphologies and crystal growth orientations were prepared for methanol-to-propylene (MTP) reactions. Despite having similar acidity, significant differences in lifetimes and selectivity were observed over the three different ZSM-5 catalysts under a high space velocity of 10 h^{-1}. Generally, the lifetime and propylene selectivity were in the order of ZSM-5-NS (300 h, 55.04%) > ZSM-5-NC (168 h, 53.34%) > ZSM-5-NF (78 h, 49.31%). A series of characterization results revealed that the superior performance of ZSM-NS was attributed to its higher ratio of framework Al distribution within the straight and sinusoidal channels favored for the alkene cycle and enhancing C_{2-4} olefin selectivity, a higher diffusion rate owing to its thinner (010) crystal plane along the *b* axis orientation, and higher crystallinity and fewer framework defects within the micropore contributed to an extended lifetime stability because of its lower coking rate. Additionally, the shaped ZSM-5-NS catalyst exhibited impressive stability and regenerability in a single-tube test, enduring an impressive long 2680 h lifespan in a single cycle and a total of 6800 h lifetime across three cycles, suggesting its significant potential for industrial application in the MTP process.

1. Introduction

Due to the growing demand for propylene and the diminishing availability of traditional feedstocks, the methanol-to-propylene (MTP) process has become a vital pathway for propylene production.[1] In this process, methanol is converted to propylene using a zeolite catalyst. Typically, the reaction takes place in a fixed bed reactor at temperatures ranging from 460 to 480 °C, and through olefin recycling, a total propylene selectivity of 66% can be achieved.[2,3] Among the different zeolite catalysts, ZSM-5 has been considered as the most successful catalyst for MTP conversion owing to its high selectivity towards propylene, unique topological structure, and adjustable acidity.[4,5] Nevertheless, the performance of ZSM-5 catalysts can be significantly influenced by their acidity, morphologies, size effect and crystal growth orientations.

For the acidity effect, Brønsted acid sites (BASs) are considered to be the active sites for olefin production.[6] In the past few decades, modification of ZSM-5 zeolites with different elements, such as phosphorus,[7] boron[8,9] or alkaline-earth metals has been shown to successively enhance the selectivity to propylene and, simultaneously, improve catalyst lifetime.[10] For instance, Gascon *et al.*[4] demonstrated that isolating Brønsted acid sites is crucial for selectively forming propylene, while the introduction of Lewis acid sites prevents coke formation, significantly prolonging catalyst lifetime. Shan investigated the effects of Si/Al molar ratios on the MTP reaction over ZSM-5 zeolites,[11] and the highest propylene selectivity (45.9%) was obtained over a ZSM-5 zeolite catalyst with SiO_2/Al_2O_3 molar ratio of 220. Li *et al.* reported a series of H-ZSM-5 zeolites with Si/Al molar ratios ranging from 50 to 4000 but have similar crystal sizes. The results showed that the selectivity to propylene consistently increased with an increasing Si/Al ratio.[12] This suggests that a high Si/Al ratio in H-ZSM-5 promotes the

[a] *Key Laboratory of Material Chemistry for Energy Conversion and Storage, Ministry of Education, Hubei Key Laboratory of Material Chemistry and Service Failure, School of Chemistry and Chemical Engineering, Huazhong University of Science and Technology, Wuhan, 430074, People's Republic of China. E-mail: klgyl@hust.edu.cn*
[b] *State Key Laboratory of Coal Conversion, Institute of Coal Chemistry, Chinese Academy of Sciences, 27th South Taoyuan Rd, Taiyuan 030001, People's Republic of China. E-mail: wuzhiwei@sxicc.ac.cn*
[c] *University of the Chinese Academy of Sciences, Beijing 100049, People's Republic of China. E-mail: wangjianguo@ucas.ac.cn*
[d] *National Energy Group Ningxia Coal Industry Co., Ltd, Yinchuan 750000, People's Republic of China*

† Electronic supplementary information (ESI) available. See DOI: https://doi.org/10.1039/d3cy01558k

‡ The authors made the same contribution to this paper.

propagation of the alkene-based methylation/cracking cycle over the arene-based methylation/dealkylation cycle in MTP.[13] Recently, Zhang *et al.* controlled the acidity of MFI-zeolites by incorporating gallium(III) centres into silicalite-1; the optimal GaS-1(1.3) zeolite exhibits simultaneously remarkable propene selectivity (45.3%), P/E ratio (14.6) and catalytic stability (>180 h) at full methanol conversion.[14]

For the crystal size effect, it has been reported that a smaller crystal size of ZSM-5 catalysts exhibits higher propylene selectivity and activity due to their increased surface area and accessibility to active sites.[15] For example, Guo *et al.*[16] developed a method to precisely control the particle sizes of boron-containing ZSM-5 catalysts, ranging from 153 nm to 14.2 μm, by adjusting the addition of silicalite-1 seeds. Compared with 14.2 μm and 676 nm, the 336 nm HZSM-5 shows better propylene selectivity and longer stability. Yao *et al.*[17] also observed that HZSM-5 zeolites with smaller crystal sizes possess a larger surface area and pore volume, a higher density of pore openings, and shorter micropore channel lengths, which help prevent side reactions. In comparison to crystal sizes of 5 μm and 1–2 μm, the smaller 100–300 nm crystal sizes of HZSM-5 exhibited increased resistance, better tolerance to coke, longer catalytic lifetime, and higher propylene selectivity.

For the morphology effect, the shape of ZSM-5 crystals has also been found to influence the catalytic performance. Song *et al.*[18] reported that an interconnected hierarchical ZSM-5 with a nano-disc shape prepared by a dealumination–realumination process is a superior MTP catalyst; the interconnected hierarchical structure and suitable acidity showed a longer lifetime of 195 h and a higher propylene selectivity of 48.8%. Yu *et al.*[19] prepared high-quality single-crystalline MFI-type nano-zeolites (10–55 nm) with hexagonalprism morphology, which deliver a lifetime of 54 h with a high propylene selectivity of 49% at 470 °C. Lu reported coffin-shaped single crystals with a thickness of 180–200 nm and a length of >1 μm, coated on stainless steel fibers, which exhibited a long-term stability of at least 1600 h (>94% conversion) and a high propylene selectivity of 36% at 450 °C.[20] Deng *et al.* designed a specific core–shell MFI zeolite, in which Al-ZSM-5 aggregates acted as the core and B-ZSM-5 or silicalite-1 as the shell; the Al-ZSM-5@B-ZSM-5 zeolite displayed more weak acid sites and few strong acid sites on its shell surface, which are beneficial for the low formation of external coke, high propylene selectivity and long lifetime.[21]

Except for the morphology, the orientation of zeolites also significantly affects the diffusion path and mass transfer of feed and product molecules, which ultimately determines the catalytic performance. In the case of ZSM-5 zeolite, it possesses a three-dimensional pore structure with interconnected straight pores (0.53 nm × 0.56 nm) along the *b*-axis and sinusoidal pores (0.51 nm × 0.55 nm) along the *a*-axis. The diffusion property of straight channels is more favorable than that of sinusoidal channels.[22] Therefore, controlling the *b*-axis thickness of ZSM-5 is crucial as it can reduce the residence time of reaction products, and inhibit hydrogen transfer, oligomerization, cyclization, aromatization, and other side reactions. It also helps reduce the rate of carbon accumulation and prolong the catalyst's lifespan. In recent years, significant progress has been made by various experts in preparing MFI zeolites with controllable *b*-axis-oriented length. For example, Ryoo *et al.*[23] synthesized 2 nm thick ZSM-5 in the *b*-axis direction by using $C_{22\text{-}6\text{-}6}$ Br_2 surfactant to restrict the growth of ZSM-5 zeolite. Xiao *et al.*[24] proposed that urea can be uniformly dispersed on the (010) surface of MFI structure molecular sieves, thereby restricting the growth of MFI crystals along the *b*-axis. They successfully reduced the thickness of TS-1 crystals along the *b*-axis from 300 nm to 80 nm by adding inexpensive urea to the TS-1 zeolite synthesis gel. Another approach involved the use of fluoride ions to prepare nanosheet ZSM-5, which successfully produced plate-like Al- and Ga-containing MFI zeolites with a short diffusion path along the *b*-axis (~60 nm). These plate-like ZSM-5 zeolites with lower acid density effectively suppressed the aromatic-based cycle and promoted the olefin-based cycle, leading to a higher selectivity to propylene in MTP conversion.[25] Li *et al.*[26] used a ZSM-5 nanosheet (NS) seed and *n*-butylamine (NBA) template to prepare twin-free nanoslab ZSM-5 zeolite with *b*-axis thickness of 60–90 nm; the nanoslab ZSM-5 showed a high 48.1% selectivity to propylene and 192 h lifetime in the MTP reaction. Luo *et al.*[27] also used a seed-induced preparation method with a silica sol solution to prepare short *b*-axis ZSM-5 nano-sheets; the best nano-sheet HT-ZSM-5-SM zeolite shows a 355 h catalytic life, and the selectivity of propylene can reach about 51%. With the exception of the *b*-axis orientation, the alignment along the *a*-axis and *c*-axis can also significantly influence the performance of ZSM-5. For instance, Wu P. *et al.* synthesized a thin nano-sheet ZSM-5 oriented along the *a*-axis, with a thickness of approximately 12 nm. This *a*-oriented ZSM-5 exhibited enhanced propylene selectivity (54% propylene) and a longer lifetime compared to bulky crystals (33% propylene) in the MTP reaction. The superior performance can be attributed to the unique morphology oriented along the *a*-axis, which shortens the zig-zag channel formed by 10-rings and facilitates a more distinct release of diffusion resistance.[28] Additionally, Xie Z. *et al.* observed that the catalytic activity and stability of sheet-like ZSM-5 are improved with a longer *c*-axis. By controlling the length of the *c*-axis, they found that an extended *c*-axis exposes a higher proportion of straight channels, which is more favorable for diffusion.[29]

All the aforementioned research studies indicate that the catalytic performance of zeolites is intricately influenced by a range of physical and chemical properties. Achieving an optimal prototype catalyst requires careful adjustment of these properties. In this study, we aimed to explore the impact of distinct morphologies and growth orientations on the performance of ZSM-5 catalysts in the MTP reaction. To achieve this, three typical morphologies of ZSM-5 with nearly identical acidity were prepared. Following an extensive testing and characterizations, the nanosheet-shaped ZSM-5-NS, characterized by a short *b*-axis growth orientation, exhibited an impressive lifetime of up to 300 h under a high

weight hourly space velocity (WHSV) of 10 h^{-1} and displayed a superior C_{2-4} olefin selectivity of 84.69%. In contrast, under the same conditions, the nanocylinder-shaped ZSM-5-NC exhibited a lifetime of 168 h and a C_{2-4} olefin selectivity of 80.73%, while the fusiform-shaped ZSM-5-NF showed the shortest lifetime of 78 h and the lowest C_{2-4} olefin selectivity of 76.81%. We deeply investigated their physicochemical properties, including pore structure, growth orientations, framework aluminum distributions, defect sites, and diffusion properties, and examined their effects on the catalytic performance of the MTP reaction.

2. Experimental

2.1 Materials

The chemicals, including tetraethyl orthosilicate (TEOS) sodium aluminate ($NaAlO_2$, AR), aluminum sulfate ($Al_2(SO_4)_3$, AR), urea ($CO(NH_2)_2$, AR), sodium hydroxide (NaOH, AR), tetrapropylammonium hydroxide (TPAOH, 25 wt% in water), and methanol (AR), were obtained from Sinopharm Chemical Reagent Co., Ltd. Silica sol (30 wt% SiO_2, 0.3 wt% Na_2O) was purchased from Qingdao Haiyang Chemical Co., Ltd. All chemicals were used as received without any purification.

2.2 Catalysts preparation

2.2.1 Synthesis of nano-sheet ZSM-5. Nano-sheet ZSM-5 zeolite was synthesized with the molar composition of 400 SiO_2 : 1 Al_2O_3 : 12 Na_2O : 120 TPAOH : 30 H_2O, from the mixture of sodium hydroxide (NaOH), silica sol, aluminum sulphate, and tetrapropylammonium hydroxide (TPAOH, 25 wt% in aqueous solution). Typically, 0.0958 g of $Al_2(SO_4)_3$ and 0.20 g of NaOH were dissolved in a solution containing 20.0 g deionized water and 26.2 g TPAOH, with vigorous stirring at room temperature. Then, 22.4 g silica sol was slowly added into the solution. The gel was then stirred vigorously for 15 minutes to ensure homogeneity. Afterward, 2.0 wt% silicalite-1 seeds, relative to the SiO_2 mass of the gel, were introduced into the system. Finally, a few drops of hydrofluoric acid were added to achieve a pH value of approximately 8.0. Once the gel was formed, it underwent aging and homogenization for 3 h. The gel was then transferred to a 100 mL Teflon-lined autoclave. Crystallization took place at 170 °C for 48 h in a Teflon-lined stainless-steel autoclave with rotation (15 r min^{-1}). The resulting solid products were recovered through centrifugation and washed repeatedly with deionized water until the pH value of the mother liquid reached 7–8. Subsequently, the solid products were dried at 100 °C overnight and calcined at 550 °C for 6 h in air. To obtain HZSM-5, the synthesized material underwent ion-exchange twice using an aqueous NH_4NO_3 solution (1 M, *m*(liquid)/*m*(solid) = 40) at 80 °C for 5 h, followed by calcination at 550 °C for 6 h. The prepared catalyst was denoted as ZSM-5-NS.

Sheet-like seed preparation.[24,30] $CO(NH_2)_2$ was added into an aqueous solution mixture of TPAOH and NaOH. Then TEOS was slowly added to the mixture while stirring. The system was stirred at room temperature for 24 h. Then, the mixture was transferred to a Teflon-lined stainless-steel autoclave and crystallized at 120 °C for 60 h. The initial composition of the gel used for the seed synthesis was SiO_2 : 0.4 TPAOH : 0.4 $CO(NH_2)_2$: 0.05 Na_2O : 40 H_2O.

2.2.2 Synthesis of nano-cylinder ZSM-5. Nano-cylinder ZSM-5 zeolite was synthesized with a molar composition of 400 SiO_2 : 1 Al_2O_3 : 12 Na_2O : 60 TPAOH : 30 H_2O. To obtain zeolites with a uniform particle size, 2.0 wt% silicalite-1 seeds, prepared by following the procedures of Li and coworkers,[31] was added to the above-mentioned synthesis gel. The crystallization was conducted at 170 °C for 40 h in a Teflon-lined stainless-steel autoclave under rotation (15 r min^{-1}). The solid products were recovered by centrifugation and washing with deionized water repeatedly until the mother liquid showed a pH value of 10, followed by drying at 110 °C overnight and calcination at 550 °C for 10 h in air. The ZSM-5 zeolite in hydrogen form (HZSM-5) was obtained through ion-exchanging for two times with aqueous NH_4NO_3 solution (1 M, *m*(liquid)/*m*(solid) = 40) at 80 °C for 5 h and subsequent calcination at 550 °C for 6 h. The prepared catalyst was denoted as ZSM-5-NC.

2.2.3 Synthesis of nano-fusiform ZSM-5. Nano-fusiform ZSM-5 zeolite was synthesized with the molar composition of 400 SiO_2 : 1 Al_2O_3 : 20 Na_2O : 40 TPAOH : 20 H_2O. To obtain zeolites with a uniform particle size, 0.5 wt% silicalite-1 seeds, prepared by following the procedures of Li and coworkers,[31] was added to the above-mentioned synthesis gel. The crystallization was conducted at 170 °C for 40 h in a Teflon-lined stainless-steel autoclave under rotation (15 r min^{-1}). The solid products were recovered by centrifugation and washing with deionized water repeatedly until the mother liquid showed a pH value of 10, followed by drying at 110 °C overnight and calcination at 550 °C for 10 h in air. The ZSM-5 zeolite in hydrogen form (HZSM-5) was obtained through ion-exchanging for two times with aqueous NH_4NO_3 solution (1 M, *m*(liquid)/*m*(solid) = 40) at 80 °C for 5 h and subsequent calcination at 550 °C for 6 h. The prepared catalyst was denoted as ZSM-5-NF.

2.2.4 MTP catalyst extrusion molding. A certain amount of ZSM-5 zeolite powder was taken and mixed thoroughly with pseudo-boehmite as a binder and talc powder as an extrusion aid. Nitric acid solution was added to the mixed powder, and the mixture was kneaded thoroughly using a twin-screw extruder to form an extruded shape. The extruded catalyst was then dried at 120 °C for 2 h and subsequently calcined at 550 °C for 4–5 h. After cooling to room temperature, cylindrical ZSM-5 zeolite catalyst particles with a diameter of 3 mm were obtained.

2.3 Catalyst characterization

Thermogravimetric (TG) analysis was carried out on a Rigaku Thermo plus Evo TG 8120 analyzer, and the samples were heated in air from room temperature to 800 °C with a heating rate of 10 °C min^{-1}.

Inductively coupled plasma optical emission spectroscopy (ICP-OES) was conducted on a Thermo iCAP 6300 ICP-OES system with a CID detector to determine actual Al and Si content.

The X-ray diffraction (XRD) patterns were collected on a powder X-ray diffractometer (Bruker AXS D8, Germany) equipped with Cu Kα radiation source (0.15406 nm) operated at 40 kV and 40 mA, in the region of 2θ = 10–40° with a scanning rate of 4° min^{-1}.

The surface area (BET) and pore diameter and volume (BJH) were analyzed on an ASAP 2010 physisorption analyzer by N_2 sorption at −196 °C. All samples were vacuum degassed at 300 °C for 8 h before each adsorption experiment. The specific surface area (S_{BET}) was determined by the Brunauer–Emmett–Teller (BET) equation. The micropore volume (V_{micro}) and external surface area (V_{ext}) were calculated by the *t*-plot method and the total pore volume (V_{pore}) was based on the adsorbed amount of N_2 at p/p_0 = 0.99. The mesopore volume (V_{meso}) was calculated by subtracting V_{micro} from the corresponding V_{pore}. The pore size distribution (PSD) was estimated by employing the Barrett–Joyner–Halenda (BJH) method from the desorption branch of the isotherm.

Transmission electron microscopy (TEM) images of all samples were taken on a JEM 2100 microscope operating at 200 kV.

Magic angle spinning (MAS) nuclear magnetic resonance (NMR) spectra of ^{27}Al were collected on an Avance III 600 MHz wide bore spectrometer from Bruker operating at a magnetic field of 14.2 T in a single pulse sequence. The chemical shifts for ^{27}Al MAS NMR spectra were referenced to the aqueous solution of $Al(NO_3)_3$ and tetramethylsilane (TMS), respectively. The ^{27}Al MAS NMR spectra were acquired at a spinning rate of 13 kHz with a π/12 pulse width of 1.2 μs and a recycle delay of 1 s; the number of scans used was 8000.

Temperature-programmed desorption of NH_3 (NH_3-TPD) was performed on a Micromeritics AutoChem II 2920 chemisorption analyzer. The catalyst sample (100 mg) was pretreated in argon stream (30 mL min^{-1}) at 500 °C for 2 h and then cooled to 120 °C, then NH_3 gas (5 vol% in argon, 30 mL min^{-1}) was introduced for 30 min to allow a saturated adsorption. After that, the sample was purged with the argon stream at 120 °C for 30 min and then heated up from 120 to 550 °C at a ramp of 10 °C min^{-1} in the argon stream, during which the amount of NH_3 desorption upon heating was recorded by a thermal conductivity detector (TCD).

Fourier transform infrared (FT-IR) absorption spectra in transmission mode were acquired on a Vertex 70 spectrometer (Bruker). The spectra were collected at room temperature with 64 scans at a resolution of 4 cm^{-1}.

STEM experiments were conducted using a double Cs-corrected microscope (FEI Titan Cubed Themis Z) operating at 300 kV. Prior to each experiment, the microscope was aligned using a cross-grating standard sample. Specimen searching and zone axis alignment were performed under the TEM mode at a magnification of 13 000×. Once the crystal zone axis was aligned, the microscope was switched to the STEM mode to capture iDPC- and HAADF-STEM images simultaneously.

2.4 Catalytic tests

2.4.1 Powder catalyst evaluation. The powder catalyst test was carried out in a fixed-bed microreactor with a diameter of 20 mm. The main process is that the powder samples were pelletized and cracked to 20–40 mesh, and after that, 2 g samples mixed with quartz sand were loaded into the fixed bed reactor. The samples were first activated in a 200 mL min^{-1} N_2 atmosphere at 470 °C for 1 h, and then passed through with a methanol feedstock. The diluted methanol (60 wt% in water) solution was used as a reaction raw material, and the reaction was carried out at a weight-hourly space velocity (WHSV) of 10 h^{-1}.

2.4.2 Single-tube evaluation of the shaped catalysts. The shaped catalyst was evaluated in a single-tube fixed-bed microreactor with a diameter of 40 mm and a length of 1200 mm. The catalyst consisted of 80 g of shaped particles with a diameter of 3.0 mm and a length ranging from 3–8 mm, which were packed along with 2 mm inert porcelain balls in the fixed bed reactor. Prior to the evaluation, the catalyst sample underwent an activation process in a nitrogen (N_2) atmosphere at a flow rate of 500 mL min^{-1} and a temperature of 480 °C for 1 hour. Following the activation, the catalyst was exposed to water steam at 480 °C for a duration of 48 h. After the steam treatment, the catalyst was cooled down to 430 °C and then subjected to a methanol feedstock in the presence of a nitrogen atmosphere with a flow rate of 1000 ml min^{-1}. The methanol feedstock used was a mixture of methanol and water, with a CH_3OH concentration of 60 wt%. The catalytic reaction was performed at a weight-hourly space velocity (WHSV) of 1.25 h^{-1}, and the bed temperature was maintained in the range of 460–485 °C.

Methanol conversion (X) and product selectivity (S) were defined as follows:

$$X = \frac{n^{in}_{MeOH} - n^{out}_{MeOH} - 2n^{out}_{DME}}{n^{in}_{MeOH}} \times 100\% \quad (1)$$

$$S = \frac{m \times n^{out}_{C_mH_n}}{n^{in}_{MeOH} - n^{out}_{MeOH} - 2n^{out}_{DME}} \times 100\% \quad (2)$$

where n is the number of moles, and m is the number of carbon atoms corresponding to C_mH_n.

2.4.3 Regeneration of catalysts. The catalyst regeneration process employs an online multi-stage regeneration method. Initially, the gas within the reactor is switched to nitrogen and purged at 450 °C for 2 h. Subsequently, the gas is switched to nitrogen with a 2% oxygen content, maintained for 10 h. The temperature is then elevated to 470 °C, and the oxygen concentration is increased to 5% for a regeneration period of 10 hours. Following this, the oxygen concentration is further increased to 10%, and the regeneration continues for another 10 h. The regeneration process is terminated when the concentration of CO_2, as determined by TCD chromatography,

falls below 50 ppm. It is crucial to note that the internal bed temperature of the reactor must not surpass 500 °C throughout the entire regeneration cycle.

2.5 Diffusion simulation

The diffusion behavior of methanol, ethene, propylene, *n*-butene, *p*-xylene, and *o*-xylene molecules within the intersection cavities, sinusoidal channels, and straight channels of H-ZSM-5 zeolite was investigated using molecular dynamics (MD) simulations conducted with the Sorption and Forcite module within the Material Studio 7.0 software, employing the canonical ensemble. The simulation temperature was maintained at 743 K and controlled using a single Nosé–Hoover thermostat with a time step of 1.0 fs. The COMPASS force field was employed, and the velocity Verlet algorithm was used to integrate Newton's equations of motion, allowing accurate representation of the diffusion and adsorption of small molecules within zeolite frameworks.[32,33] Methanol, ethene, propylene, *n*-butene, *p*-xylene, and *o*-xylene molecules were placed within a 3 × 3 × 3 supercell of H-ZSM-5 zeolite (with lattice parameters a = 60.066 Å, b = 59.697 Å, and c = 40.149 Å), and all atoms involved, including those in the zeolite framework, underwent full relaxation. Prior to the MD simulations, all geometries were optimized. Trajectories were recorded at intervals of 500 steps during the production stage of the simulation.

3. Results and discussion

3.1 Morphology and structural features

Fig. 1 illustrates three typical morphologies of ZSM-5 zeolites. All types of ZSM-5 zeolites in the SEM exhibit high monodispersity without any adhesion, which is crucial for efficient diffusion. In Fig. 1a-1, ZSM-5-NS displays a regular hexagonal nano-sheet shape with a thickness ranging from 40–100 nm, a width of approximately 120–250 nm, and a length of about 1–1.5 μm. In Fig. 1b-1, ZSM-5-NC exhibits a cylindrical shape with uniform dispersion, having a thickness of around 150–200 nm and a diameter of 250 nm. Additionally, ZSM-5 zeolite in Fig. 1c-1 demonstrates a fusiform shape with a size of 1 μm. TEM analysis confirms the observations made in the SEM images, further validating the morphological characteristics of the ZSM-5 samples, and the growth orientations of the crystal plane were marked respectively. The selected area electron diffraction (SAED) results indicate that all the synthesized ZSM-5 samples, despite their different morphologies, maintain a single crystal structure. It is worth noting that the crystal integrity decrease in the order of ZSM-5-NS > ZSM-5-NC > ZSM-5-NF.

3.2 Textural properties and crystallinity

In Fig. 2, the XRD patterns of all the samples exhibit distinct and highly crystalline diffraction peaks characteristic of the MFI-type structure, without any impurities. As shown in the figure, the characteristic diffraction peaks of the MFI topology appear at 2θ = 7.95°, 8.90°, 23.24°, 23.92°, and 24.38°, corresponding to the crystal surfaces of (101), (020), (051), (033), and (133), respectively.[34] The main difference among the three different ZSM-5 samples lies in the relative intensities of the diffraction lines, particularly those corresponding to the (020) reflections. ZSM-5-NS exhibits the strongest intensity for the (020) diffraction peak, ZSM-5-NC exhibits the middle intensity, while ZSM-5-NF shows the

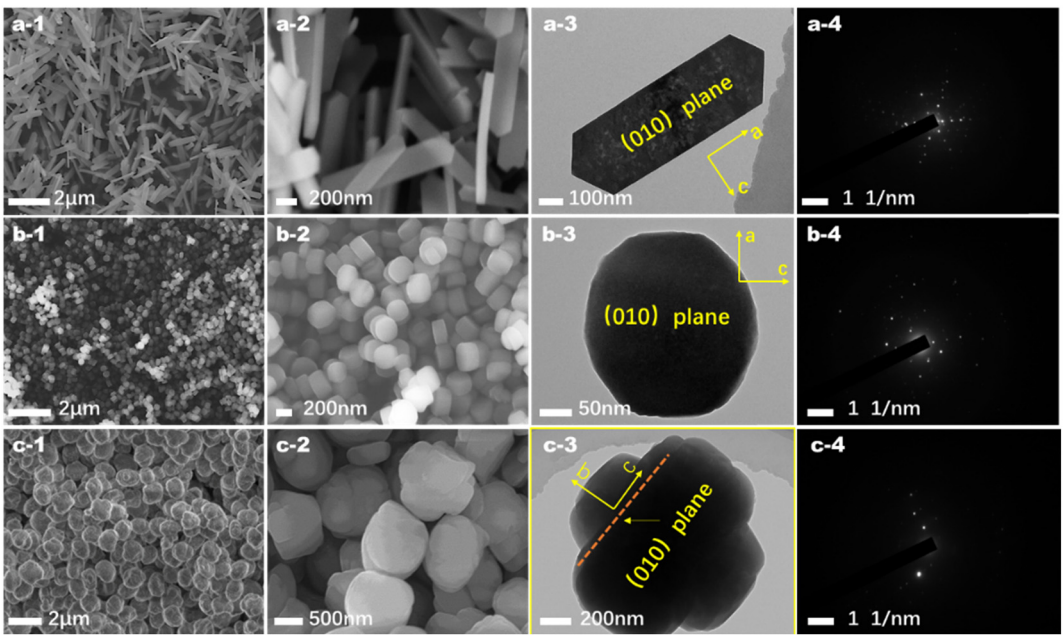

Fig. 1 SEM, TEM, and corresponding selected area electron diffraction (SAED) images of the as-synthesized ZSM-5 samples with different morphologies. (a.1–4) ZSM-5-NS; (b.1–4) ZSM-5-NC; (c.1–4) ZSM-5-NF.

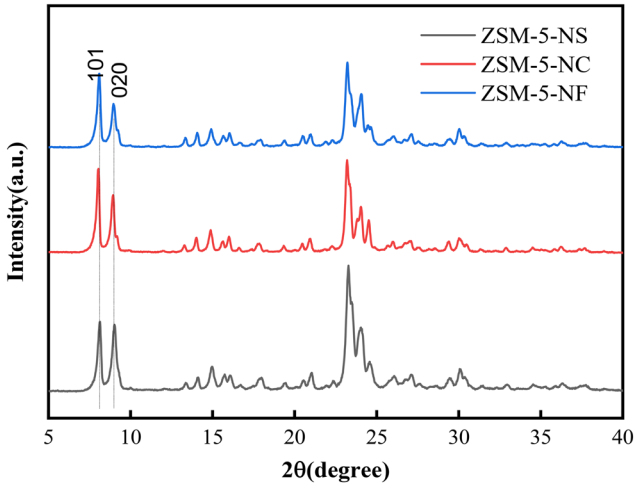

Fig. 2 XRD patterns of the calcined ZSM-5 samples with different morphologies.

lowest intensity. The observed variation in the relative intensities of the diffraction lines, particularly the (020) peak, can be attributed to the presence of preferential crystal planes associated with different morphologies of ZSM-5, which is consistent with the SEM and TEM results.

Table 1 provides the physical properties of these three ZSM-5 morphologies. It can be observed that the Si/Al molar ratios are nearly identical, but ZSM-5-NC shows the largest BET surface area, 375.3 $m^2\ g^{-1}$, along with the highest values of $n_{(S_{External}/S_{Micro})}$ and micropore volume, indicating the presence of a larger external surface area in the nano-sized ZSM-5-NC. In comparison, ZSM-5-NF exhibits a smaller external surface area, likely due to its larger size. ZSM-5-NS falls in between ZSM-5-NC and ZSM-5-NF in terms of S_{BET} and $n_{(S_{External}/S_{Micro})}$. The crystallinity of the three samples in the table follows the order: ZSM-5-NS > ZSM-5-NC > ZSM-5-NF, which is consistent with the TEM SAED results. This indicates that ZSM-5-NS exhibits the highest degree of crystallinity among the three samples, followed by ZSM-5-NC and ZSM-5-NF. The TEM analysis supports this observation and confirms that ZSM-5-NS possesses a more well-defined and ordered crystal structure compared to ZSM-5-NC and ZSM-5-NF.

Fig. 3 presents the nitrogen sorption isotherms of these three HZSM-5 samples. As shown in Fig. 3a, all H-ZSM-5 samples display high microporosity, characterized by significant uptake steps at relatively low pressures ($p/p^0 < 0.02$). ZSM-5-NS and ZSM-5-NC exhibit features of traditional microporous materials with type I isotherm curves, and we have not found obvious mesopores in Fig. 3b for ZSM-5-NS. On the other hand, the isotherm of ZSM-5-NF is noticeably different, displaying a modified type IV isotherm with an apparent hysteresis loop at p/p^0 = 0.30–0.99, which suggests irregular mesoporosity arising from the voids between the particles.

Fig. 4 displays the TEM image of ZSM-5-NS, which confirms its hexagonal nanosheet morphology. Additionally, Fig. 4a clearly shows the presence of randomly distributed mesopores within the ZSM-5-NS crystals, with pore diameters ranging from 10 to 40 nm. The iDPC-STEM image in Fig. 4b shows the projection view along the (010) direction, providing evidence that the *b*-axis (representing the straight channels) is the shortest dimension of the crystal. FFT diffractograms of H-ZSM-NS substantiate its high quality single crystalline structure, which is consistent with the SEM, TEM and XRD results. Fig. 4h shows that the thickness of H-ZSM-5-NS is about 80 nm; HR-TEM and SAED images in Fig. 4i and j proved that the side of H-ZSM-5-NS is the [100] plane from the *a*-axis orientation.

3.3 Acidity

The acidity of the ZSM-5 zeolites was characterized by NH_3-TPD and Py-IR spectroscopy. Fig. 5a illustrates the NH_3 desorption profiles for the three samples, showing two distinct peaks. NH_3 desorption peaks in the temperature ranges of 150–200 °C and 350–400 °C represent NH_3 adsorbed on weak and strong acid sites, respectively. Quantitative analysis of NH_3-TPD results is presented in Table 2. It can be observed that the total acidity of the three samples is comparable due to their similar Si/Al ratio. However, there are differences in acid strength. The ZSM-5-NF exhibits higher desorption temperatures for both weak acid (167.7 °C) and strong acid (352.4 °C) peaks compared to ZSM-5-NC and ZSM-5-NS. This can be attributed to the larger size of ZSM-5-NF, which hinders the desorption and diffusion of NH_3 molecules. The Brønsted acid and Lewis acid properties of the three catalysts were also investigated by pyridine infrared spectroscopy, and the results demonstrated that the three catalysts exhibited similar B acid and L acid properties based on the pyridine infrared spectra. The peak positions and intensities associated with B acids and L acids were comparable across all three catalysts, indicating similar acidity characteristics.

Acidity changes of the samples were also studied by FT-IR spectroscopy in the hydroxyl-stretch vibration regions, as shown in Fig. 6. There are four main IR bands in the region of 3800–3600 cm^{-1}. The first one at 3732 cm^{-1} corresponds to external free silanol groups, and the band at 3720 cm^{-1} is

Table 1 Physical properties of the prepared ZSM-5 catalysts

Samples	S_{BET}[a] ($m^2\ g^{-1}$)	S_{Micro}[a] ($m^2\ g^{-1}$)	$S_{External}$[a] ($m^2\ g^{-1}$)	$n_{(S_{External}/S_{Micro})}$	Micropore volume[a] ($cm^3\ g^{-1}$)	Si/Al[b] molar ratio	Crystallinity[c] (%)
ZSM-5-NS	359.3	299.4	59.5	0.20	0.1232	198.5	100
ZSM-5-NC	375.3	293.8	81.4	0.27	0.1345	201.3	95
ZSM-5-NF	364.5	317.2	47.3	0.15	0.1237	200.5	92

[a] Measured by the *t*-plot method. [b] Measured by ICP. [c] Crystallinity was calculated from the representative peak area of the XRD diffraction.

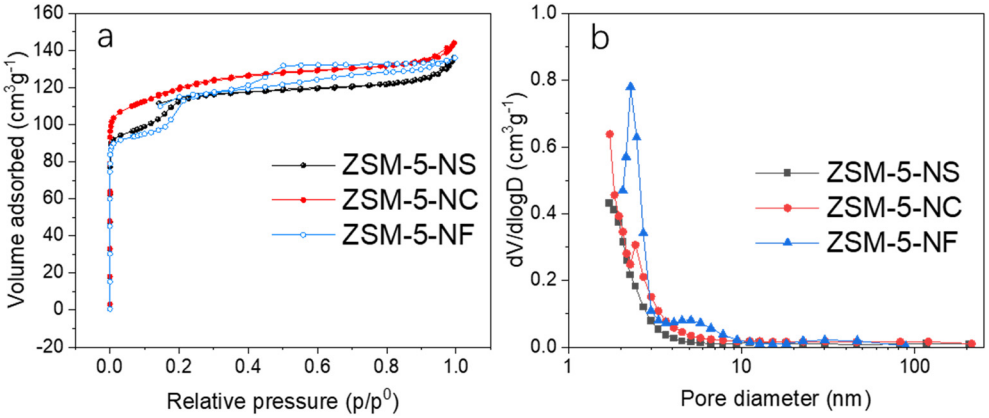

Fig. 3 N_2 adsorption–desorption isotherms and the corresponding pore size distribution of the three samples. (a) N_2 isotherms of ZSM-5, (b) pore size distributions of ZSM-5.

attributed to internal (defective) silanol groups. A smaller band at 3650 cm^{-1} belongs to extraframework aluminum hydroxyls.[18] Another major band at 3600 cm^{-1} could be ascribed to Brønsted acid sites Si(OH)Al.

Previous studies have shown a correlation between the formation of coke deposits and the presence of silanol defects. For example, Thibault-Starzyk *et al.*[35] found that coke deposits were primarily located on non-acidic silanol groups within the micropore system during the isomerization of *ortho*-xylene. Barbera *et al.*[36] also highlighted the importance of internal framework defects in the deactivation behavior of ZSM-5 catalysts in the methanol to gasoline reaction. They observed a clear correlation between the deactivation rate and the intensity ratio of IR bands corresponding to internal silanols at 3726 cm^{-1} and external silanol groups at 3745 cm^{-1}. Additionally, Sazama *et al.*[37] confirmed the correlation

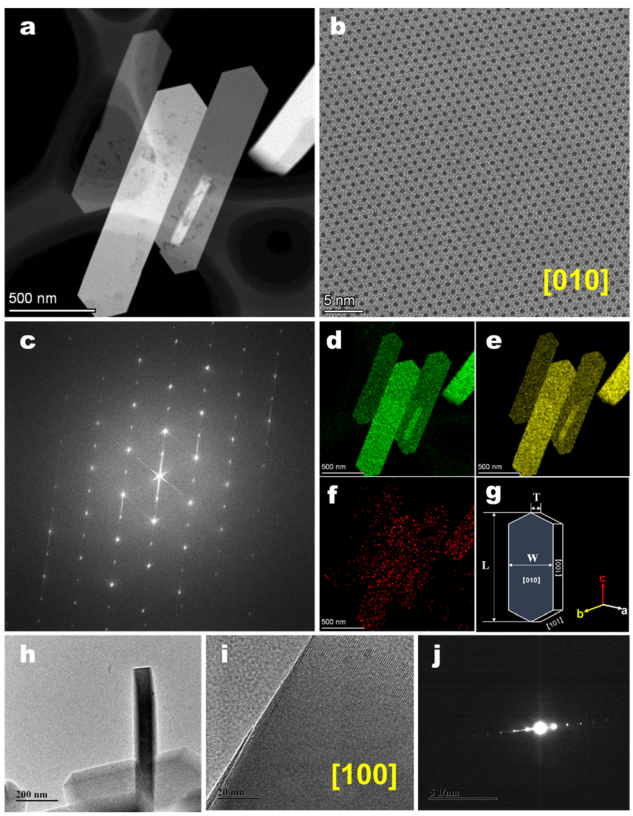

Fig. 4 (a) TEM image of HZSM-5-NS, (b) iDPC-STEM image of the (010) surface, (c) corresponding FFT diffractograms of HZSM-NS, (d) Si element mapping, (e) O element mapping, (f) Al element mapping, (g) schematic map of the nano-sheet crystal dimensions and the corresponding crystal faces, (h) TEM image of the (100) plane, (i) HR-TEM image of the (100) surface, and (j) SAED image of the (100) plane.

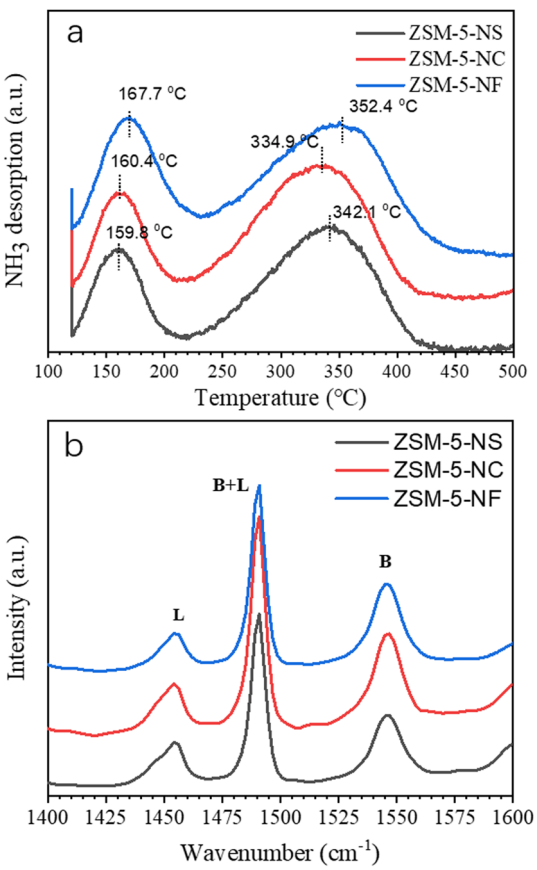

Fig. 5 NH_3-TPD and Py-IR of the as-synthesized ZSM-5 samples with different morphologies. (a) NH_3-TPD, (b) Py-IR.

Table 2 Quantitative analysis results of NH_3-TPD and Py-IR from the ZSM-5 samples with different morphologies

	Acidity by NH_3-TPD ($\mu mol\ g^{-1}$)			Acidity by Py-IR ($\mu mol\ g^{-1}$)		
Samples	Weak	Strong	Total	Brønsted	Lewis	Total
ZSM-5-NS	41	88	129	60	18	78
ZSM-5-NC	43	92	135	63	19	82
ZSM-5-NF	44	90	134	61	18	79

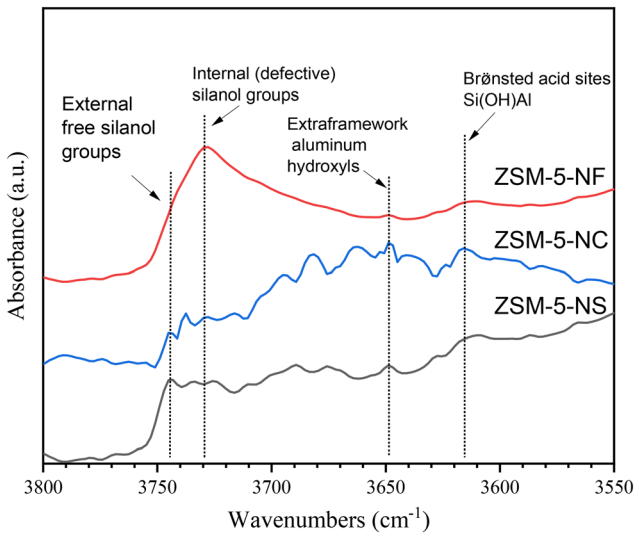

Fig. 6 FTIR spectra in the OH-stretch region (3800–3550 cm^{-1}) of the samples with different morphologies.

between framework defects in H-ZSM-5 and the catalyst's lifetime in MTH using a combination of IR and solid-state NMR spectroscopy.

In this study, the ZSM-5-NS catalyst exhibits the largest number of external silanol groups and the fewest internal silanol groups. This can be attributed to the high-quality single crystalline structure of the nano-sheet-shaped ZSM-5, as observed in the TEM results in Fig. 4. The ZSM-5-NS catalyst thus has minimal internal framework silanol defects. On the other hand, the fusiform-shaped ZSM-5-NF catalyst displays the fewest external silanol groups and the largest number of internal silanol groups due to its larger size (approximately 1 μm) and lower crystallinity. Compared to ZSM-5-NS and ZSM-5-NF, the nano-cylinder-shaped ZSM-5-NC catalyst exhibits intermediate values of external and internal silanol groups. These difference between three samples may also originated from the different morphology and different methods.

3.4 Catalytic performance

To evaluate the catalytic activities, MTP reactions over the three different zeolite samples were carried out with WHSV of 10 h^{-1}. The catalyst deactivation was defined as the running time from the beginning of the 100% methanol conversion to the conversion decreasing around 95%. The methanol conversion and propylene selectivity as a function of time on stream over three samples are shown in Fig. 7 parts a–c, respectively. All catalysts show complete conversion of methanol in the initial period, indicating initial high activity. As a comparison, ZSM-5-NS exhibits the longest catalytic lifetime (300 h), much longer than that of ZSM-5-NC (168 h) and ZSM-5-NF (78 h). Table 3 lists the MeOH conversion and product mean selectivity and coking rate of the MTP reactions of H-ZSM-5 with different morphologies; it can be seen that the $C_{2-4}^{=}$ selectivity over H-ZSM-5 with different morphologies is in the order of ZSM-5-NS > ZSM-5-NC > ZSM-5-NF, with about 84.69% > 80.73% > 76.81% respectively. Meanwhile, the C_{5+} and aromatic selectivity follows the order ZSM-5-NS < ZSM-5-NC < ZSM-5-NF. The higher $C_{2-4}^{=}$ selectivity and longer lifetime of ZSM-5-NS can be attributed to its faster diffusion rate, which is a result of two factors: the much thinner crystal face from the (010) plane and the higher crystallinity compared to ZSM-5-NC and ZSM-5-NF. The thinner (010) crystal plane along the *b* axis provides shorter diffusion pathways for reactants and products, facilitating their movement within the zeolite structure. Additionally, the higher crystallinity of ZSM-5-NS ensures a more ordered and well-defined pore structure, enabling efficient diffusion of molecules and minimizing diffusion limitations.[38] These factors contribute to improved performance and longevity of ZSM-5-NS compared to ZSM-5-NC and ZSM-5-NF.

To further investigate the deactivation process, we measured the variations in textural properties and coking rate, as shown in Fig. 7(e and f) and Table 3. The results indicate that ZSM-5-NS exhibited the lowest coking rate, approximately 0.115 wt%/h, while ZSM-5-NF demonstrated the highest coking rate of 0.137 wt%/h. Additionally, ZSM-5-NS also showed the slowest decline rate in BET surface area and micropore volume during the catalytic lifetime. These findings suggest that ZSM-5-NS is more resistant to coking and maintains its textural properties better compared to ZSM-5-NC and ZSM-5-NF.

Catalyst deactivation by coking is a critical issue that affects the lifetime of the MTP process. To further investigate the reasons for deactivation in the three samples with different morphologies, a thermogravimetric (TG) test was conducted on the deactivated catalysts. In a typical MTP fixed-bed reactor, the catalyst bed can be divided into three sections: the deactivation section, methanol conversion section, and olefins conversion section, corresponding to the top, middle, and bottom of the reaction tube, respectively. Fig. 8 presents the weight loss curves of the spent catalysts through TG analysis. As depicted in the figure, the weight loss of the deactivated samples can be divided into two stages: 50–200 °C and 200–700 °C. The first stage corresponds to the desorption of water, unreacted methanol or dimethyl ether, and other volatile components, while the second stage represents the loss of coke deposited on the deactivated samples. In Fig. 8, the amount of coke deposition

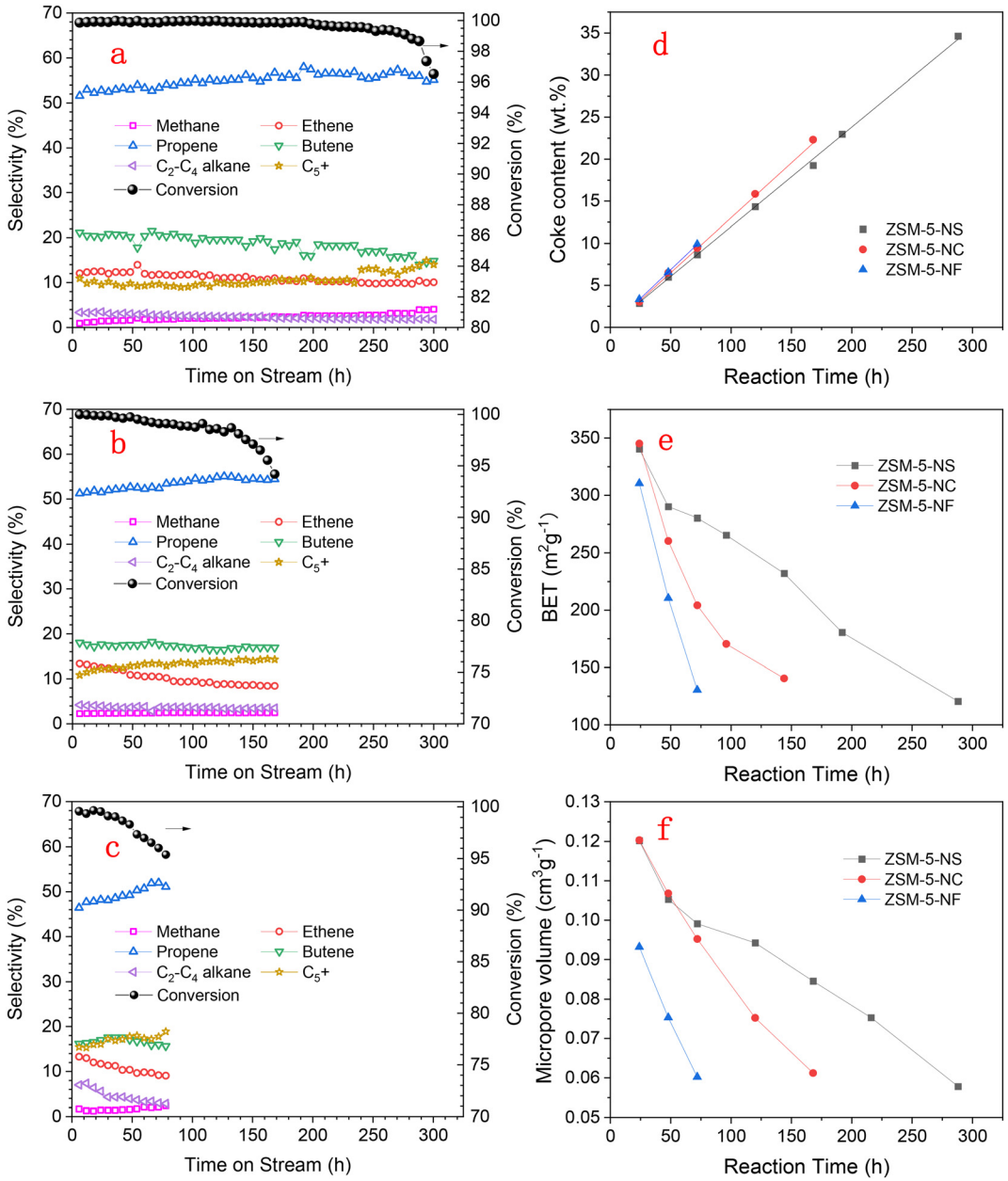

Fig. 7 Methanol conversion of methanol and MTP selectivity as a function of time-on-stream over ZSM-5-NS, ZSM-NC and ZSM-5-NF with different morphologies. (a) ZSM-5-NS, (b) ZSM-5-NC, (c) ZSM-5-NF, (d) coke content *vs.* reaction time, (e) BET variation *vs.* reaction time, and (f) micropore volume variation *vs.* reaction time. Reaction conditions: catalyst, 2.0 g; T = 475 °C; WHSV = 10 h^{-1}.

Table 3 MeOH conversion and product selectivity and coking rate of the MTP reactions of H-ZSM-5 with different morphologies

Samples	Life time (h)	Product mean selectivity (%)									Coking rate[b] (wt%/h)
		CH_4	C_2H_4	C_3H_6	C_4H_8	$C^{=}_{2-4}$	C^{0}_{2-4}	C_{5+}[a]	Arom.	P/E	
ZSM-5-NS	300	2.30	11.04	55.04	18.61	84.69	2.37	10.63	5.82	4.99	0.115
ZSM-5-NC	168	2.41	10.18	53.34	17.21	80.73	3.63	13.23	6.89	5.23	0.132
ZSM-5-NF	78	1.67	10.82	49.31	16.68	76.81	4.56	17.01	8.96	4.56	0.137

[a] C_5 and higher hydrocarbons including aromatics. [b] Calculated by the TG result.

on the different ZSM-5 samples follows the order: ZSM-5-NS (34.63%) > ZSM-5-NC (19.36%) > ZSM-5-NF (9.21%). This indicates that ZSM-5-NS exhibits better catalytic performance due to fewer defective sites and higher carbon capacity. Fig.

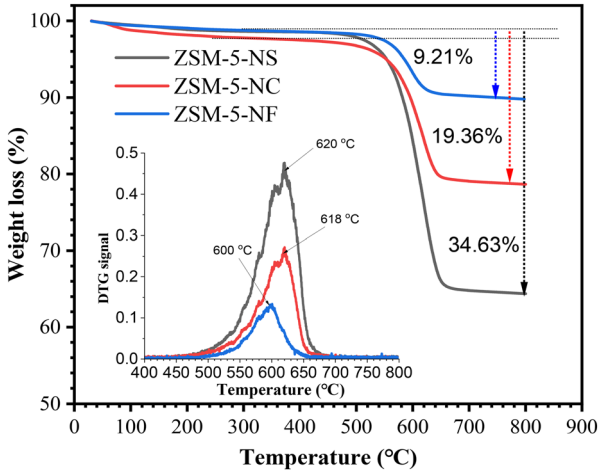

Fig. 8 TG profiles of the as-synthesized ZSM-5 samples with different morphologies.

S1† shows the TEM of coke deposition species over ZSM-5 with different morphologies, as can be seen, the coke deposited species on the zeolite surface is amorphous carbon.

According to the literature,[39] the coke fractions associated with carbonaceous structures can be classified into three groups by differential thermogravimetry (DTG): group 1 represents coking on the external surface of the zeolite (burned off at 350–450 °C); group 2 corresponds to coking at the mouth of zeolite micropores (burned off at 450–500 °C); group 3 indicates coking within the internal micropores of the zeolite (burned off above 500 °C). The burn-off temperature of coke follows the order: group 1 < group 2 < group 3. This implies that coke deposited on the external surface of the zeolite is more easily burned off compared to coke at the mouth of zeolite micropores and within the internal micropores of the zeolite. In this study, the DTG burn-off temperature represents the coking structures and their loading location. In the inset of Fig. 8, the DTG curve shows the burned-off temperature as follows: ZSM-5-NS (620 °C) > ZSM-5-NC (618 °C) > ZSM-5-NF (600 °C). This indicates that all three catalysts have coking primarily deposited in the micropores due to their high Si/Al molar ratio. However, ZSM-5-NS exhibits a larger peak and higher temperature, indicating a higher amount of coking in the micropores compared to ZSM-5-NC and ZSM-5-NF. This is the reason why ZSM-5-NS demonstrates a larger capacity and longer lifetime compared to the other samples.

Raman spectroscopy is commonly employed for characterizing and analyzing structural information about carbonaceous deposits on catalysts. In particular, the characteristic peaks at 1600 and 1350 cm^{-1} are associated with highly ordered graphitic carbonaceous deposits and disordered aromatic hydrocarbon species, respectively.[40] The I_D/I_G ratio is often utilized to quantify the degree of graphitization in carbonaceous materials, where a lower value indicates a higher degree of graphitization in the carbonaceous deposits. Fig. S2 and Table S1† shows that the degree of graphitization order of the coking was as follows: ZSM-5-NS < ZSM-5-NC < ZSM-5-NF, which indicates a lower degree of graphitization in the carbonaceous deposits within the micropores of ZSM-5, this is another reason why ZSM-5-NS has longer lifetime than others.

3.5 Diffusion of methanol, alkenes, and aromatics in H-ZSM-5

As is known, diffusion plays a crucial role in determining the selectivity and lifetime of zeolite catalysts. Thus, to delve into the diffusion behavior of methanol, ethene, propylene, *n*-butene, *p*-xylene, and *o*-xylene within the sinusoidal channels and straight channels of H-ZSM-5 zeolite, we employed MD simulations using the Material Studio 7.0 software. The detailed results are presented in Fig. 9. In this illustration, density maps were generated based on two-dimensional projections of the mass centers of guest molecules within a 3 × 3 × 3 supercell. The color bars denote the density of guest molecules distributed across different channels, with a unit of 1. The red regions, characterized by higher density values, indicate a greater likelihood of diffusion. The *Y*-axis direction denotes the straight channel, while the *X*-axis direction pertains to the sinusoidal channel. As observed from the figure, smaller molecules like methanol, ethene, propylene, and *n*-butene exhibit easier diffusion in both the straight and sinusoidal channels of ZSM-5. On the other hand, larger molecules such as *p*-xylene and *o*-xylene tend to diffuse predominantly within the straight channels. This observation aligns with the longer lifetime of the nano-sheet ZSM-5-NS zeolite in the MTP reaction, attributed to its thinner (010) crystal plane exposure and elevated crystallinity.

To further investigate the diffusion rates of various ZSM-5 morphologies, vapor adsorption isotherms of *o*-xylene were conducted on different ZSM-5 morphologies, and the results are presented in Fig. S3.† As depicted in the figure, ZSM-5-NS exhibited the highest adsorption rate and saturation capacity, followed by ZSM-5-NC, and ZSM-5-NF demonstrated the slowest diffusion rate and the lowest adsorption saturation capacity. These disparities can be attributed to differences in morphologies, grain sizes, and crystal orientations. The experimental diffusion results align well with simulation results, TG results and the assessment of MTP catalyst lifetimes.

3.6 Location and distribution of Al atoms within the ZSM-5 zeolite framework

Except for the diffusion, the location and distribution of Al atoms within the zeolite framework have emerged as significant factors affecting the catalyst's activity and selectivity.[41] As is known, the Brønsted acid site properties of aluminosilicate-type zeolites are originated from the presence of protons that balance the negative charge generated by the framework aluminum (Al_F) atoms in tetrahedral sites (T-sites).[42] For example, more acid sites appeared in the

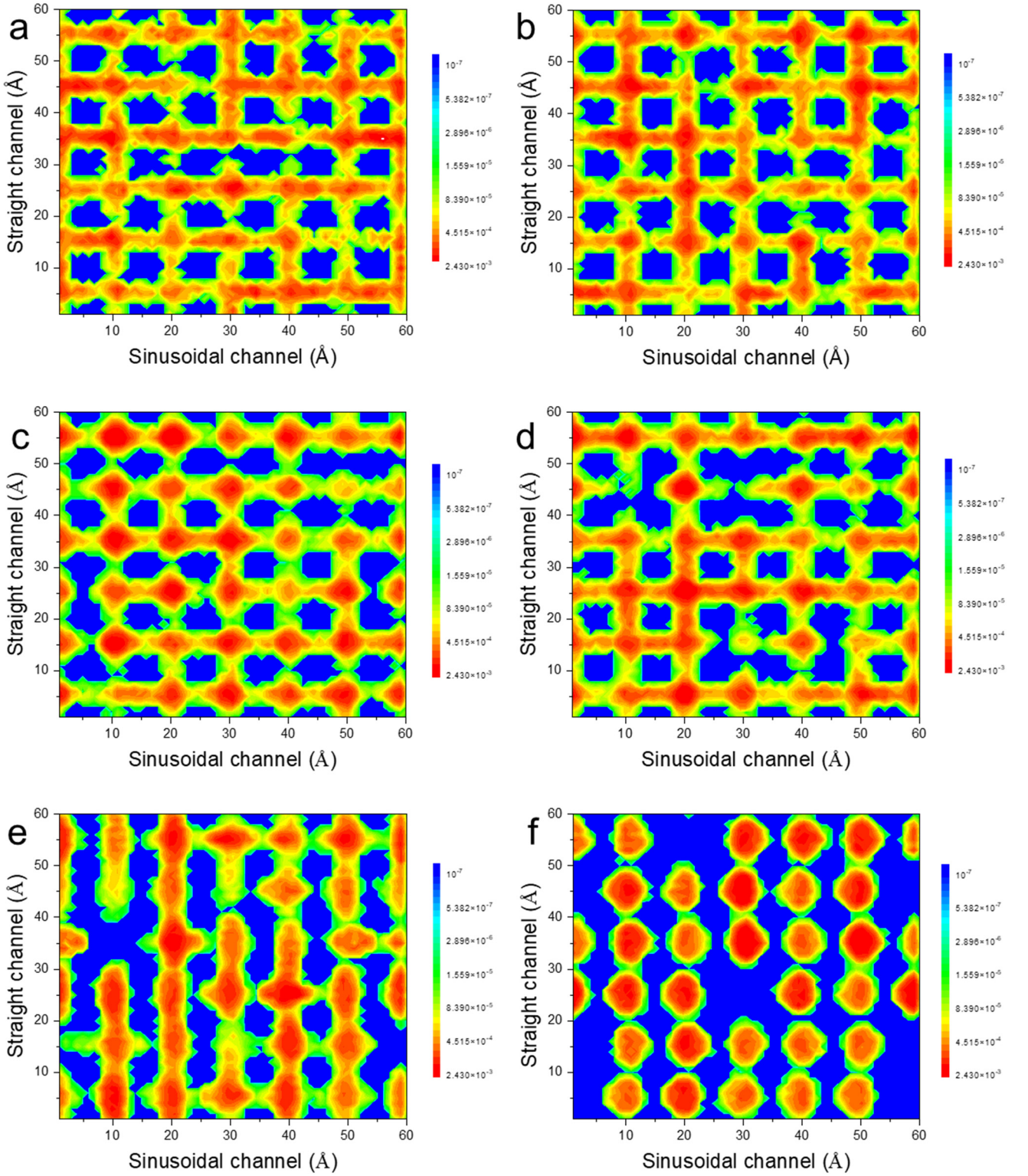

Fig. 9 Contour lines for the diffusion of (a) methanol, (b) ethene, (c) propylene, (d) *n*-butene, (e) *p*-xylene, and (f) *o*-xylene molecules in the straight and sinusoidal channels of H-ZSM-5 zeolite at 743 K.

supercage and/or intersection cavity of zeolites can relatively enhance the aromatics cycle and produce more ethene and aromatic species, whereas the acid sites siting in the 10-membered ring (10-MR) channel are more encouraging for the propagation of the alkene cycle, thus preferentially generating propylene and butene.[9,43]

Therefore, in order to investigate the distribution of Al_F in relation to different morphologies of ZSM-5 in the MTP

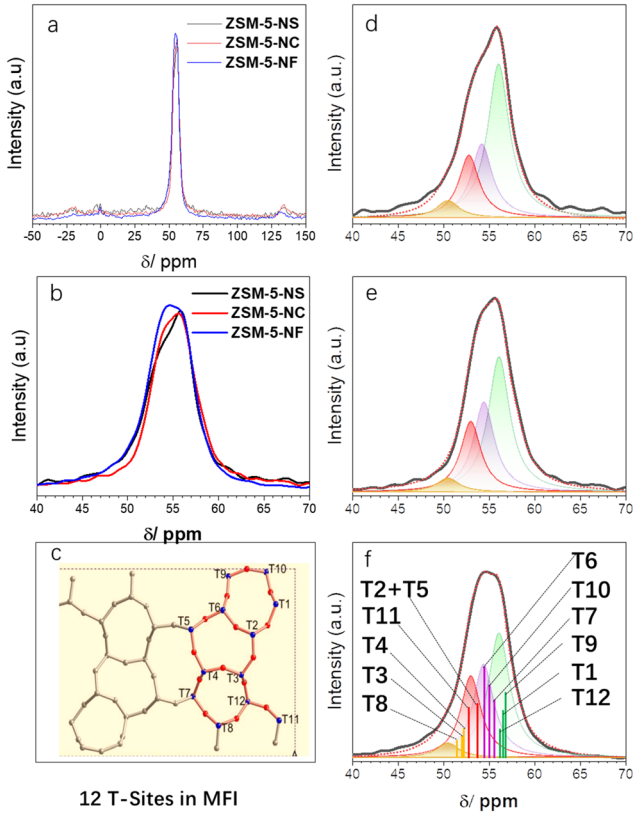

Fig. 10 ^{27}Al MAS NMR spectra of ZSM-5 with different morphologies, (a) low magnification, (b) high magnification, and (c) crystallographically distinct 12 T-sites in the MFI structure,[44] (d) peak fitting of ZSM-5-NS, (e) peak fitting of ZSM-5-NC, and (f) peak fitting of ZSM-5-NF.

reaction, ^{27}Al magic angle spinning (MAS) NMR spectroscopy was conducted to characterize Brønsted acid sites the within the micropores of the MFI framework. Fig. 10 illustrates the ^{27}Al (MAS) NMR spectra of ZSM-5 zeolites with different morphologies. In Fig. 10a, a low magnification spectrum is shown, providing an overview of the spectral features. Fig. 10b presents high magnification spectra, allowing for a closer examination of the peaks. It can be seen from the figure, the broad peaks of different morphologies of ZSM-5 ranging from 45–70 ppm are different. The difference in the peaks would be caused by the different distribution of Al atoms over 12 distinct T-sites of the MFI structure. To better understand the precise positions of the 12 T-sites, the crystallographically distinct T-sites in the MFI structure of ZSM-5 are illustrated in Fig. 10c. In order to analyze the NMR spectra in greater detail, peak fitting was conducted for each sample, as shown in Fig. 10d–f. Utilizing the ^{27}Al MAS NMR spectra, the broad peak ranging from 45 to 65 ppm, attributed to the framework Al atoms, was divided into four peaks around 56, 54, 53, and 52 ppm.[45] These peaks are designated as Al_F-a, Al_F-b, Al_F-c, and Al_F-d, respectively, and their proportions are listed in Table 4. Fig. 10d presents the peak fitting results for ZSM-5-NS, Fig. 10e displays the peak fitting results for ZSM-5-NC, and Fig. 10f showcases the peak fitting results for ZSM-5-NF. The peak fitting analysis provides valuable insights, indicating that ZSM-5-NS and ZSM-5-NC possess a higher ratio of T-sites located in straight 10-MR channels and sinusoidal 10-MR, while ZSM-5-NF exhibits a higher proportion of T-sites located at the intersections. In our previous DFT calculation work had predicted that if the fractions of sinusoidal and straight channel acid sites were higher, the alkene cycle was relatively favored, which enhanced selectivity for propylene and higher alkenes; if the number of intersection cavity acid sites of H-ZSM-5 zeolite was higher, the formation of aromatic intermediates would be promoted, the aromatic cycle would be favored, and, therefore, the ethene-to-propylene ratio in the MTO conversion products would be increased.[46] Our earlier experiment demonstrated that more ethene and aromatic species could be produced on H-ZSM-5 zeolite with a higher number of intersection cavity acid sites, which was prepared using tetraethyl orthosilicate as the Si source, whereas H-ZSM-5 with a higher number of straight and sinusoidal channel acid sites, which was prepared using silica sol as the Si source, presented higher selectivity for propylene and C_{3+} alkenes.[41] These results were well matched our catalytic data in Fig. 10 and Table 4, as we found that ZSM-5-NS and ZSM-5-NC show higher propylene selectivity due to them possessing a higher proportion of Al_F acid sites in the sinusoidal (T1 + T6 + T9 + T10 + T2) and straight channel (T3 + T4 + T8 + T12), according to Fig. 10c, while ZSM-5-NF has more Al_F acid sites in the intersection and follow the aromatic cycle (T5 + T7), so it exhibits a lower propylene selectivity for olefins, P/E value and higher aromatics in the test. This observation was also in agreement with results of Kim *et al.* in the MTP reaction.[47]

3.7 Single-tube test and regeneration stability

In industrial applications, solid catalysts need to exhibit specific shapes and sizes to fit seamlessly within catalytic reactors while minimizing pressure drop. Therefore, these solid catalysts commonly undergo shaping processes to attain

Table 4 Peak fitting data of ^{27}Al MAS NMR spectra of ZSM-5 with different morphologies

Peaks	Al_F-a	Al_F-b	Al_F-c	Al_F-d
T-sites	T1 + T9 + T12	T7 + T10 + T6	T2 + T5 + T11	T3 + T8 + T4
Chemical shift (ppm)	56.3–56.8	54.4–55.6	52.6–53.8	51.7–52.3
ZSM-5-NS	51.80%	23.40%	19.00%	5.70%
ZSM-5-NC	45.50%	28.40%	21.50%	4.60%
ZSM-5-NF	41.90%	28.90%	24.40%	4.80%

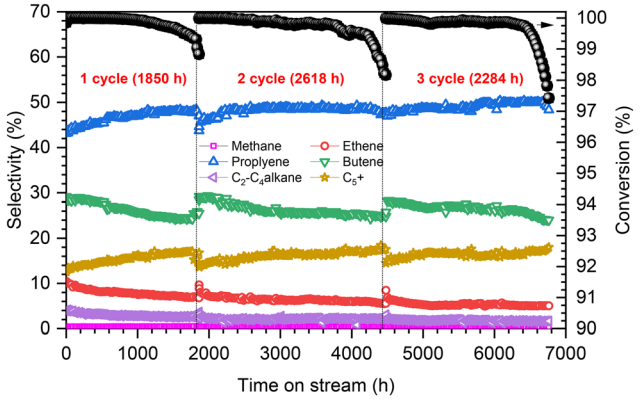

Fig. 11 Methanol conversion of methanol as a function of time on stream over shaped ZSM-5-NS. Reaction conditions: T = 460–480 °C, WHSV = 1.25 h^{-1}, catalyst weight = 80 g.

the intended configurations and dimensions before being packed. It is important to note that the shaping procedure of catalysts is intricately intertwined with their activity and plays a vital role in determining their suitability for industrial implementation.

In this study, ZSM-5-NS was extruded into a cylindrical shape with a diameter 3.0 mm and lengths ranging from 5–10 mm. This shaped catalyst was then assessed in a single-tube reactor with an 80 g (125 mL) catalyst load. The catalytic test result, as illustrated in Fig. 11, revealed that under a weight-hourly space velocity (WHSV) of 1.25 h^{-1} and within a temperature range of 460–480 °C, the shaped catalyst exhibited a lifetime of 1850 h during the initial cycle. It showed an average propylene selectivity of 46.47% and a C_{2-4} olefin selectivity of 80.05%. Following catalyst regeneration, the reaction's lifetime surged to 2618 h, accompanied by a propylene selectivity of 48.21% and a C_{2-4} olefin selectivity of 81.01%. In the third cycle, the reaction's duration extended to approximately 2284 h, with a propylene selectivity of 49.02% and a C_{2-4} olefin selectivity of 81.05%. These results proved that the shaped nano-sheet catalyst exhibited remarkable stability and regenerability, accumulating a total of 6800 h over three cycles, which was also confirmed in the ^{27}Al MAS NMR spectra of ZSM-5 with various morphologies under high temperature water steam treatment at 600 °C and 700 °C, as depicted in Fig. S4.†

4. Conclusion

In this work, three different ZSM-5 catalysts with distinct morphologies and growth orientations were synthesized for MTP by using different methods. The catalyst evaluation results demonstrated significant differences in their lifetimes and selectivity despite similar acidity among the three catalysts. The nanosheet-shaped ZSM-5-NS, characterized by a short *b*-axis growth orientation, exhibited an impressive lifetime of up to 300 h under a high weight hourly space velocity (WHSV) of 10 h^{-1} and displayed a superior propylene selectivity of 55.04% and C_{2-4} olefin selectivity of 84.69%. Under the same condition, the nanocylinder-shaped ZSM-5-NC exhibited a lifetime of 168 h and a propylene selectivity of 53.34% and C_{2-4} olefin selectivity of 80.73%, while the fusiform-shaped ZSM-5-NF showed the shortest lifetime of 78 h and the lowest propylene selectivity of 49.31% and C_{2-4} olefin selectivity of 76.81%. The superior performance of the nano-sheet catalyst can be attributed to several factors:

Firstly, compared with ZSM-5-NC and ZSM-5-NF, ZSM-5-NS displayed a notably elevated distribution ratio of framework Al_F within the straight and sinusoidal channels, a configuration that is conducive to promoting the alkene cycle. This distinctive feature played a pivotal role in enhancing its C_{2-4} olefin selectivity, and extremely for the propylene selectivity.

Secondly, ZSM-5-NS displayed a higher diffusion rate, allowing for enhanced mass transfer and improved reactant accessibility, owing to its thinner (010) crystal plane along the *b* axis orientation, which was proved by diffusion simulation and *o*-xylene vapor adsorption.

Thirdly, ZSM-5-NS exhibited higher crystallinity and fewer framework defects within the micropore structure resulted in a lower coking rate, further contributing to its superior lifetime performance.

Finally, the shaped nano-sheet catalyst demonstrated exceptional stability and regenerability during a single-tube test, showing a total 6800 h lifetime in three cycles. Notably, this achievement required fewer cycles compared to commercial MTP catalysts, which typically demand 6–8 cycles to attain similar longevity. These compelling results underscore the significant potential of the shaped nano-sheet catalyst for practical industrial applications in the MTP process.

Author contributions

Wei Zhang: conceptualization, methodology, investigation, writing original draft, and visualization; Xiaohu Wang: methodology, characterization, and investigation; Zhiwei Wu: project administration, methodology, writing – review & editing, supervision, and funding acquisition; Zhikai Li: diffusion simulation, characterization, and visualization; Xiaojing Yong: methodology, investigation, and project administration; Yanlong Gu: conceptualization, resources, project administration, funding acquisition, and writing – review & editing supervision; Jianguo Wang: conceptualization, resources, writing – review & editing, supervision, project administration, and funding acquisition.

Conflicts of interest

The authors declare that they have no known competing financial interests or personal relationships that could have appeared to influence the work reported in this paper.

Acknowledgements

The authors are grateful to the National Key Research and Development Project [2022YFE0124100, 2020YFB0606404,

2020YFA0210902], the National Natural Science Foundation of China [21902054, 22072049 and 22172184], the Fundamental Research Project of ICC-CAS [SCJC-DT-2022-04, SCJC-DT-2023-01], the Foundation of State Key Laboratory of Coal Conversion [J24-25-603], the Ordos Key Research and Development Project [2022EEDSKJZDZX003], the Innovation and Talent Recruitment Base of New Energy Chemistry and Device [B21003], and the HUST Academic Frontier Youth Team [2019QYTD06].

References

1 F. L. Bleken, S. Chavan, U. Olsbye, M. Boltz, F. Ocampo and B. Louis, *Appl. Catal., A*, 2012, **447–448**, 178–185.
2 H. Koempel and W. Liebner, in *Studies in Surface Science and Catalysis*, ed. F. Bellot Noronha, M. Schmal and E. Falabella Sousa-Aguiar, Elsevier, 2007, vol. 167, pp. 261–267.
3 E. Ebadzadeh, M. H. Khademi and M. Beheshti, *Chem. Eng. J.*, 2021, **405**, 126605–126619.
4 I. Yarulina, K. De Wispelaere, S. Bailleul, J. Goetze, M. Radersma, E. Abou-Hamad, I. Vollmer, M. Goesten, B. Mezari, E. J. M. Hensen, J. S. Martinez-Espin, M. Morten, S. Mitchell, J. Perez-Ramirez, U. Olsbye, B. M. Weckhuysen, V. Van Speybroeck, F. Kapteijn and J. Gascon, *Nat. Chem.*, 2018, **10**, 804–812.
5 C. Mei, P. Wen, Z. Liu, H. Liu, Y. Wang, W. Yang, Z. Xie, W. Hua and Z. Gao, *J. Catal.*, 2008, **258**, 243–249.
6 U. Olsbye, S. Svelle, M. Bjørgen, P. Beato, T. V. W. Janssens, F. Joensen, S. Bordiga and K. P. Lillerud, *Angew. Chem., Int. Ed.*, 2012, **51**, 5810–5831.
7 J. Liu, C. Zhang, Z. Shen, W. Hua, Y. Tang, W. Shen, Y. Yue and H. Xu, *Catal. Commun.*, 2009, **10**, 1506–1509.
8 Y. S. Yang, C. Sun, J. M. Du, Y. H. Yue, W. M. Hua, C. L. Zhang, W. Shen and H. L. Xu, *Catal. Commun.*, 2012, **24**, 44–47.
9 J. Tuo, S. B. Fan, N. W. Yang, S. P. Cheng, D. Wang, J. L. Zhang, Q. X. Ma, X. H. Gao and T. S. Zhao, *Catal. Sci. Technol.*, 2020, **10**, 7034–7045.
10 M. Stöcker, *Microporous Mesoporous Mater.*, 1999, **29**, 3–48.
11 R. C. Wei, C. Y. Li, C. H. Yang and H. H. Shan, *J. Nat. Gas Chem.*, 2011, **20**, 261–265.
12 H.-W. Huang, H. Zhu, S.-H. Zhang, Q. Zhang and C.-Y. Li, *J. Fuel Chem. Technol.*, 2019, **47**, 74–82.
13 J. S. Martínez-Espín, K. De Wispelaere, T. V. W. Janssens, S. Svelle, K. P. Lillerud, P. Beato, V. Van Speybroeck and U. Olsbye, *ACS Catal.*, 2017, **7**, 5773–5780.
14 L. Zhang, R. Tu, G. Q. Ren, Z. Li, S. L. Zhai, Y. C. Xu and T. Yu, *Chem. Eng. J.*, 2023, **458**, 141447–141456.
15 M. Firoozi, M. Baghalha and M. Asadi, *Catal. Commun.*, 2009, **10**, 1582–1585.
16 C. Y. Dai, J. J. Li, A. F. Zhang, C. H. Nie, C. S. Song and X. W. Guo, *RSC Adv.*, 2017, **7**, 37915–37922.
17 M. Yao, S. Hu, J. Wang, T. Dou and Y. P. Wu, *Acta Phys.-Chim. Sin.*, 2012, **28**, 2122–2128.
18 J. J. Li, M. Liu, X. W. Guo, S. T. Xu, Y. X. Wei, Z. M. Liu and C. S. Song, *ACS Appl. Mater. Interfaces*, 2017, **9**, 26096–26106.
19 Q. Zhang, G. Chen, Y. Wang, M. Chen, G. Guo, J. Shi, J. Luo and J. Yu, *Chem. Mater.*, 2018, **30**, 2750–2758.
20 J. Ding, P. Chen, S. Fan, Z. Zhang, L. Han, G. Zhao, Y. Liu and Y. Lu, *ACS Sustainable Chem. Eng.*, 2017, **5**, 1840–1853.
21 Y. L. Zhai, S. L. Zhang, Y. S. Shang, Y. Song, W. X. Wang, T. Ma, L. M. Zhang, Y. J. Gong, J. Xu and F. Deng, *Catal. Sci. Technol.*, 2019, **9**, 659–671.
22 J. Caro, M. Noack, J. Richter-Mendau, F. Marlow, D. Petersohn, M. Griepentrog and J. Kornatowski, *J. Phys. Chem.*, 1993, **97**, 13685–13690.
23 M. Choi, K. Na, J. Kim, Y. Sakamoto, O. Terasaki and R. Ryoo, *Nature*, 2009, **461**, 246–249.
24 Z. Shan, H. Wang, X. Meng, S. Liu, L. Wang, C. Wang, F. Li, J. P. Lewis and F.-S. Xiao, *Chem. Commun.*, 2011, **47**, 1048–1050.
25 W. Dai, L. Zhang, R. Liu, Z. Huo and N. Guan, *Mater. Today Sustain.*, 2023, **22**, 100364–100373.
26 Y. Sun, S. Cao, J. Wang, H. Tang, Z. Yang, T. Ma, Y. Gong, G. Mo and Z. Li, *ACS Sustainable Chem. Eng.*, 2022, **10**, 9431–9442.
27 A. Xing, N. Zhang, D. Yuan, H. Liu, Y. Sang, P. Miao, Q. Sun and M. Luo, *Ind. Eng. Chem. Res.*, 2019, **58**, 12506–12515.
28 R. Peng, S. Li, Z. Wan, Z.-Q. Wang, X. Si, J. Tuo, H. Xu, Y. Guan, J. Jiang, Y. Ma, X. He, X.-Q. Gong and P. Wu, *ACS Appl. Mater. Interfaces*, 2023, **15**, 28116–28124.
29 X. Liu, J. Shi, G. Yang, J. Zhou, C. Wang, J. Teng, Y. Wang and Z. Xie, *Commun. Chem.*, 2021, **4**, 107.
30 N. Wang, Y. Hou, W. Sun, D. Cai, Z. Chen, L. Liu, B. Ge, L. Hu, W. Qian and F. Wei, *Appl. Catal., B*, 2019, **243**, 721–733.
31 Q. Li, B. Mihailova, D. Creaser and J. Sterte, *Microporous Mesoporous Mater.*, 2000, **40**, 53–62.
32 C. Wang, B. Li, Y. Wang and Z. Xie, *J. Energy Chem.*, 2013, **22**, 914–918.
33 H. Sun, *J. Phys. Chem. B*, 1998, **102**, 7338–7364.
34 W. Fan, B. Fan, X. Shen, J. Li, P. Wu, Y. Kubota and T. Tatsumi, *Microporous Mesoporous Mater.*, 2009, **122**, 301–308.
35 F. Thibault-Starzyk, A. Vimont and J.-P. Gilson, *Catal. Today*, 2001, **70**, 227–241.
36 K. Barbera, F. Bonino, S. Bordiga, T. V. W. Janssens and P. Beato, *J. Catal.*, 2011, **280**, 196–205.
37 P. Sazama, B. Wichterlova, J. Dedecek, Z. Tvaruzkova, Z. Musilova, L. Palumbo, S. Sklenak and O. Gonsiorova, *Microporous Mesoporous Mater.*, 2011, **143**, 87–96.
38 P. Losch, A. B. Pinar, M. G. Willinger, K. Soukup, S. Chavan, B. Vincent, P. Pale and B. Louis, *J. Catal.*, 2017, **345**, 11–23.
39 T. Cordero-Lanzac, A. Ateka, P. Pérez-Uriarte, P. Castaño, A. T. Aguayo and J. Bilbao, *Ind. Eng. Chem. Res.*, 2018, **57**, 13689–13702.
40 J. Song, W. Shen, J. Wang and W. Fan, *Carbon*, 2016, **109**, 505–516.
41 T. Liang, J. Chen, Z. Qin, J. Li, P. Wang, S. Wang, G. Wang, M. Dong, W. Fan and J. Wang, *ACS Catal.*, 2016, **6**, 7311–7325.
42 L. Ren, B. Wang, K. Lu, R. Peng, Y. Guan, J.-g. Jiang, H. Xu and P. Wu, *Chin. J. Catal.*, 2021, **42**, 1147–1159.
43 S. Wang, L. Zhang, S. Li, Z. Qin, D. Shi, S. He, K. Yuan, P. Wang, T.-S. Zhao, S. Fan, M. Dong, J. Li, W. Fan and J. Wang, *J. Catal.*, 2019, **377**, 81–97.

44 T. Yokoi, H. Mochizuki, S. Namba, J. N. Kondo and T. Tatsumi, *J. Phys. Chem. C*, 2015, **119**, 15303–15315.
45 O. H. Han, C. S. Kim and S. B. Hong, *Angew. Chem., Int. Ed.*, 2002, **41**, 469–472.
46 S. Wang, Z. Li, Z. Qin, M. Dong, J. Li, W. Fan and J. Wang, *Chin. J. Catal.*, 2021, **42**, 1126–1136.
47 S. Kim, G. Park, M. H. Woo, G. Kwak and S. K. Kim, *ACS Catal.*, 2019, **9**, 2880–2892.